

Nonclassical photon number distribution in a superconducting cavity under a squeezed drive

S. Kono¹, Y. Masuyama¹, T. Ishikawa¹, Y. Tabuchi¹, R. Yamazaki¹, K. Usami¹, K. Koshino², and Y. Nakamura^{1,3}

¹*Research Center for Advanced Science and Technology (RCAST),*

The University of Tokyo, Meguro-ku, Tokyo 153-8904, Japan

²*College of Liberal Arts and Sciences, Tokyo Medical and Dental University, Ichikawa, Chiba 272-0827, Japan and*

³*Center for Emergent Matter Science (CEMS), RIKEN, Wako, Saitama 351-0198, Japan*

(Dated: February 21, 2017)

A superconducting qubit in the strong dispersive regime of a circuit quantum electrodynamics system is a powerful probe for microwave photons in a cavity mode. In this regime, a qubit spectrum is split into multiple peaks, with each peak corresponding to an individual photon number in the cavity (discrete ac Stark shift). Here, we measure the qubit spectrum in the cavity that is driven continuously with a squeezed vacuum field generated by a Josephson parametric amplifier. By fitting the qubit spectrum with a model which takes into account the finite qubit excitation power, the photon number distribution, which is dissimilar from the apparent peak area ratio in the spectrum, is determined. The photon number distribution shows the even-odd photon number oscillation and quantitatively fulfills Klyshko's criterion for the nonclassicality.

Advancement of the superconducting quantum circuit technologies [1] and the concept of circuit quantum electrodynamics (QED) [2] have led to the emergence of microwave quantum optics, enabling us to generate and characterize nonclassical states of electromagnetic fields in the microwave domain.

One of the most widely studied nonclassical states as a resource in quantum technologies is a squeezed vacuum [3]. In microwave quantum optics, a squeezed vacuum is conveniently generated by degenerated parametric down conversion in a Josephson parametric amplifier (JPA) based on the nonlinearity of Josephson junctions [4, 5]. Characterizations of such states propagating in a waveguide have been realized by measuring the quadrature amplitudes with a homodyne technique using a JPA [6] or a cryogenic HEMT amplifier [7, 8]. JPAs and related circuits are also used to generate and characterize two-mode squeezing in spatially or spectrally separated propagating modes [9–13]. More recently, it has been shown that a squeezed vacuum injected in a cavity induces nontrivial effects to the relaxations of a qubit [14, 15] and a spin ensemble [16]. In the Fock basis, on the other hand, a squeezed vacuum displays another feature of the nonclassicality, i.e., the photon number distribution composed of only even photon numbers [17]. In the optical domain, direct observations of the photon number distribution using a photon-number-resolving detector were reported [18, 19]. In the microwave domain, however, because of the smallness of the energy of a single photon, photon counting in a propagating mode is still a challenging task, while a few realizations of microwave single-photon detectors have been reported [20–22].

Here, we report the measurement of the photon number distribution for a squeezed vacuum field continuously injected into a cavity containing a superconducting qubit. In the strong dispersive regime of the circuit-QED architecture, the spectrum of the superconducting qubit is

split into multiple peaks, with each peak corresponding to a different photon number in the cavity [23, 24]. Furthermore, it is known that the peak area ratio in the qubit spectrum obeys the photon number distribution [25]. In practice, however, we find unwanted effects of the finite qubit drive power, which give discrepancies between the observed peak area ratio and the actual photon number distribution in the cavity. We demonstrate a scheme to deduce the latter by comparing the spectrum with a numerical calculation. The determined photon number distribution confirms its nonclassicality by Klyshko's criterion, quantitatively indicating the even-odd photon number oscillation [26]. This is a steady-state realization and characterization of a nonclassical photon number distribution in a cavity driven continuously with a squeezed vacuum field. Owing to the input-output relation [27], the photon number distribution in the cavity can be interpreted as that of the injected microwave state in the propagating mode. It is in stark contrast with the dynamical generations and characterizations of nonclassical states (e.g., cat states) in a cavity [28, 29].

We use a circuit-QED system in the strong dispersive regime, where a transmon qubit is mounted at the center of a three-dimensional superconducting cavity as shown schematically in Fig. 1(a). Setting $\hbar = 1$, the qubit-cavity coupled system is described by the Hamiltonian

$$\mathcal{H} = \omega_c a^\dagger a + \frac{\omega_q}{2} \sigma_z - \chi a^\dagger a \sigma_z, \quad (1)$$

where $a^\dagger(a)$ is the creation (annihilation) operator of the cavity mode, σ_z is the Pauli operator of the transmon qubit, $\omega_c/2\pi = 10.4005$ GHz is the cavity resonant frequency, $\omega_q/2\pi = 8.7941$ GHz is the qubit resonant frequency, and $\chi/2\pi = 3.9$ MHz is the dispersive shift. Note that the Hamiltonian is truncated to the subspace of the ground state $|g\rangle$ and the first excited state $|e\rangle$ of the transmon qubit; the higher excited states of the qubit are not populated in the experiment below. The total

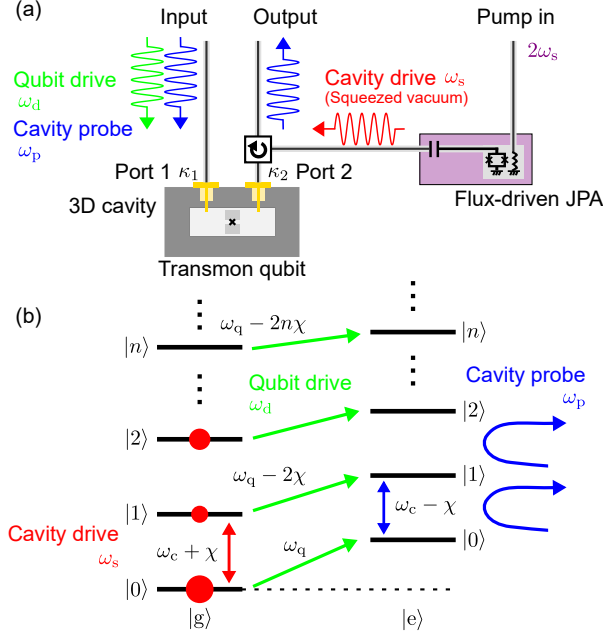


FIG. 1. (a) Schematic of the experimental setup with squeezed vacuum injection. A squeezed vacuum generated by a flux-driven Josephson parametric amplifier (JPA), as a cavity drive field ω_s , is injected into the cavity from port 2. The cavity probe field ω_p and the qubit drive field ω_d are input from port 1, and the transmission of the cavity probe field ω_p is measured. The cavity is designed to have asymmetric external coupling rates of $\kappa_2 \approx 100 \times \kappa_1$. For the thermal- and coherent-state injections, the connection to the JPA is switched to a heavily attenuated microwave line connected to the source at room temperature. (b) Energy levels of a dispersively coupled qubit-cavity system. $|g\rangle$ and $|e\rangle$ label the ground and the first excited states of the transmon qubit, and $|n\rangle$ ($n = 0, 1, 2, \dots$) indicates the photon number states of the cavity. The cavity drive field ω_s generate the steady-state photon number distribution in the cavity (red dots).

decay rate of the cavity is $\kappa/2\pi = 0.5$ MHz, the relaxation time of the qubit is $T_1 = 5.5 \mu\text{s}$, and the dephasing time of the qubit is $T_2^* = 4.5 \mu\text{s}$, determined respectively from independent measurements. As shown in Fig. 1(b), the dispersive interaction produces both the qubit-state-dependent shift of the cavity resonant frequency and the photon-number-dependent light shift of the qubit resonant frequency (discrete ac Stark shift).

In our experiment, three inputs of continuous microwaves are used: the cavity drive, the qubit drive and the cavity probe (see Fig. 1). The cavity drive field, whose frequency ω_s is fixed at the cavity resonant frequency $\omega_c + \chi$ for the qubit in the ground state, is injected to the cavity to generate the steady-state photon number distribution. The qubit drive field ω_d is applied in order to excite the qubit depending on the photon number distribution in the cavity. The cavity probe field, whose frequency ω_p is fixed around the cavity resonant frequency,

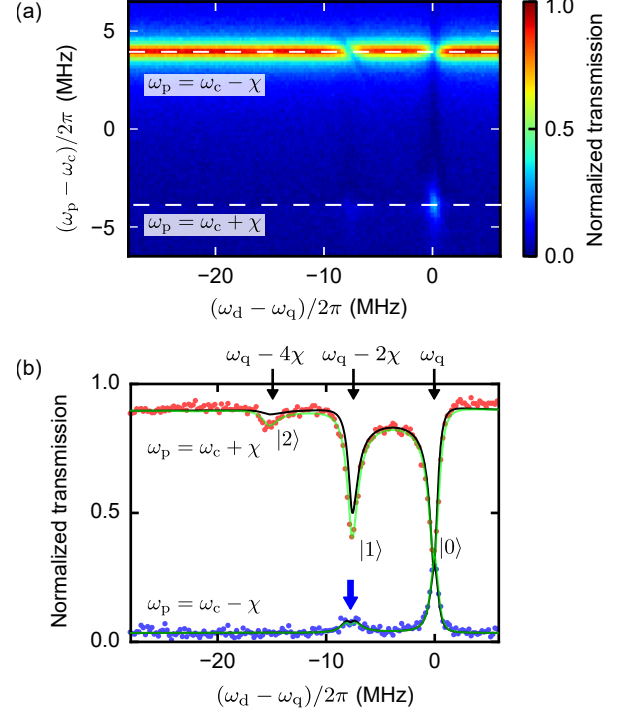


FIG. 2. (a) Cavity transmission as a function of the qubit drive frequency ω_d and the cavity probe frequency ω_p . The transmission is normalized by the maximum peak value. White dashed lines indicate $\omega_p = \omega_c \pm \chi$. (b) Cross sections of (a) at $\omega_p = \omega_c \pm \chi$ (red and blue dots, respectively). Green lines represent the rigorous numerical results in which the finite cavity probe power is fully incorporated, whereas the black lines represent the numerical results within the linear response to the cavity probe field ω_p , which corresponds to the weak power limit of the cavity probe field. The splitting of the single-photon peak, which is observed for $\omega_p = \omega_c - \chi$ (blue arrow), is understood as the Autler-Townes effect of the qubit, driven strongly at $\omega_d = \omega_q - 2\chi$ (see [30] for the details).

is used to probe the transmission of the cavity depending on the the qubit excitation probability. By measuring the cavity transmission as a function of the qubit drive frequency ω_d , we can observe the qubit spectrum reflecting the photon number distribution in the cavity. As the cavity drive fields ω_s , we compare thermal states, coherent states, and squeezed vacuum states. Thermal states are generated by amplifying the thermal noise at room temperature, and coherent states are generated by a microwave source at room temperature. They are led to the cavity through a series of attenuators to suppress the background noise. Squeezed vacuum states are generated by pumping a flux-driven JPA [31] at twice the JPA resonant frequency as shown in Fig. 1(a). The correlated photon pairs, generated from each single pump photon, show the even-odd photon number oscillation in the photon number distribution. Note that a squeezed vacuum

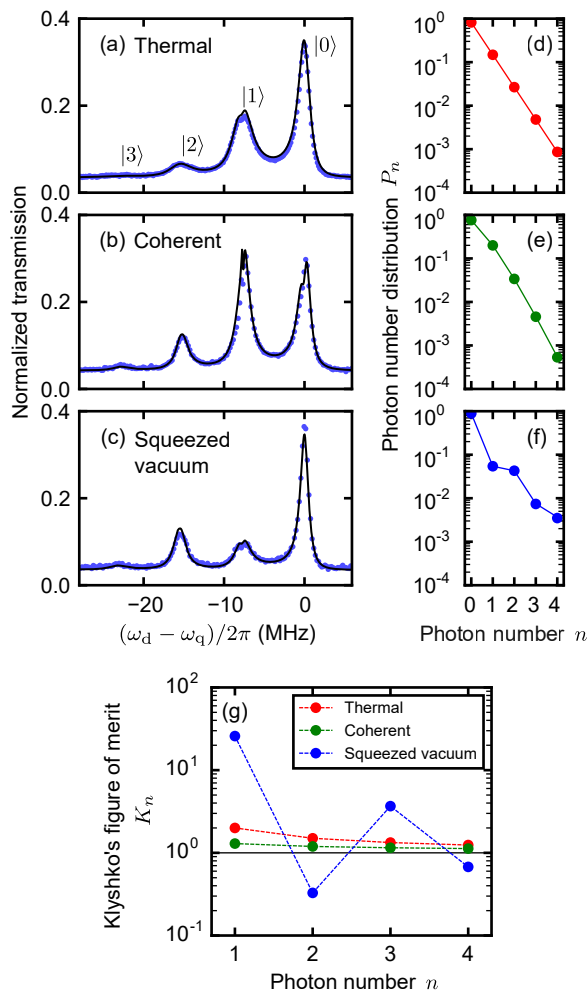


FIG. 3. (a)-(c) Qubit spectra reflecting the photon number distributions in the cavity. The cavity drive fields ω_s are in (a) thermal, (b) coherent, and (c) squeezed vacuum states, respectively. Blue dots are the experimental data, and the black solid lines are the numerically calculated linear responses. (d)-(f) Photon number distributions determined from the fittings (dots). Solid lines are the photon number distributions calculated from the corresponding models. (g) Klyshko's figures of merit K_n evaluated for each drive.

field propagating through a waveguide is in a bandwidth broader than the cavity, and the photon pairs are generated symmetrically in frequency with respect to the center frequency of the squeezed vacuum field due to energy conservation.

Before going to the main topic, we study the effect of the cavity probe field ω_p on the qubit spectra. In Fig. 2(a), we plot the cavity transmission as a function of the cavity probe frequency ω_p and the qubit drive frequency ω_d . Red (blue) dots in Fig. 2(b) depict the cross-section at $\omega_p = \omega_c + \chi$ ($\omega_p = \omega_c - \chi$) of the color plot in Fig. 2(a), respectively. Despite the absence of the cavity drive field ω_s , we observe unexpected dips and peaks

corresponding to single or double photon occupation in the cavity. Nevertheless, the numerical results, which take into account the finite cavity probe power, reproduce them very well (green lines). The excess dips in the spectrum at $\omega_p = \omega_c + \chi$ are induced by the back-action of the cavity probe field ω_p on the cavity transmission. On the other hand, for $\omega_p = \omega_c - \chi$ (cavity resonant frequency for the qubit in the excited state), the back-action is minimal. Note that the small single-photon peak still remains due to the thermal background noise, corresponding to the average photon number $n_{\text{th}} = 0.04$ in the cavity. Black solid lines in Fig. 2(b) represent the numerical results within the linear response to the cavity probe field ω_p . The deviation of the linear response from the observed spectrum is smaller at $\omega_p = \omega_c - \chi$ than at $\omega_p = \omega_c + \chi$. For the measurements below, we fix the cavity probe frequency $\omega_p = \omega_c - \chi$ which does not influence the cavity states significantly and apply the linear-response analysis.

The qubit spectra obtained in the cavity driven by different states of microwave fields are shown in Figs. 3(a)-(c). The numerical calculations (black solid lines) reproduce well the experimental results (blue dots). Dots in Figs. 3(d)-(f) represent the photon number distributions in the cavity, determined from the numerical fits for the spectra. The even-odd photon number oscillations are observed both in the qubit spectrum and in the photon number distribution for the squeezed vacuum state [Figs. 3(c) and (f)]. We estimate the quantum states of the cavity mode from the determined photon number distributions. Red line in Fig. 3(d) is the distribution corresponding to a thermal state with the average photon number $n_{\text{th}} = 0.22$. Green line in Fig. 3(e) is the distribution of a thermal coherent state with $n_{\text{th}} = 0.04$ and the displacement parameter $\alpha = 0.49$. Blue line in Fig. 3(f) is the distribution of a squeezed vacuum state with the squeezing parameter $r = 0.54$ and the loss ratio $l = 0.42$ [30]. This corresponds to a 2.1-dB squeezed state. Note that the determined photon number distributions have much less weights for larger n than the apparent peak area ratio in the qubit spectra. This is because the qubit excitation rate and the cavity decay rate are larger than the qubit decay rate. In the steady-state measurement, once the qubit is excited, the population is accumulated in $|e, 0\rangle$, which enhances the cavity transmission signal conditioned to the qubit excited state more than the actual photon number distributions for larger n .

To verify the nonclassicality of the photon number distribution under the squeezed drive, we evaluate Klyshko's figures of merit $K_n = \frac{(n+1)P_{n-1}P_{n+1}}{nP_n^2}$ ($n = 1, 2, \dots$) [26] shown in Fig. 3(g). K_n gives the nonclassicality criterion which can be calculated with the photon number distribution alone. If one of K_n is less than one, the state is nonclassical. As shown in Fig. 3(g), in the case of squeezed vacuum state, K_n becomes below unity for

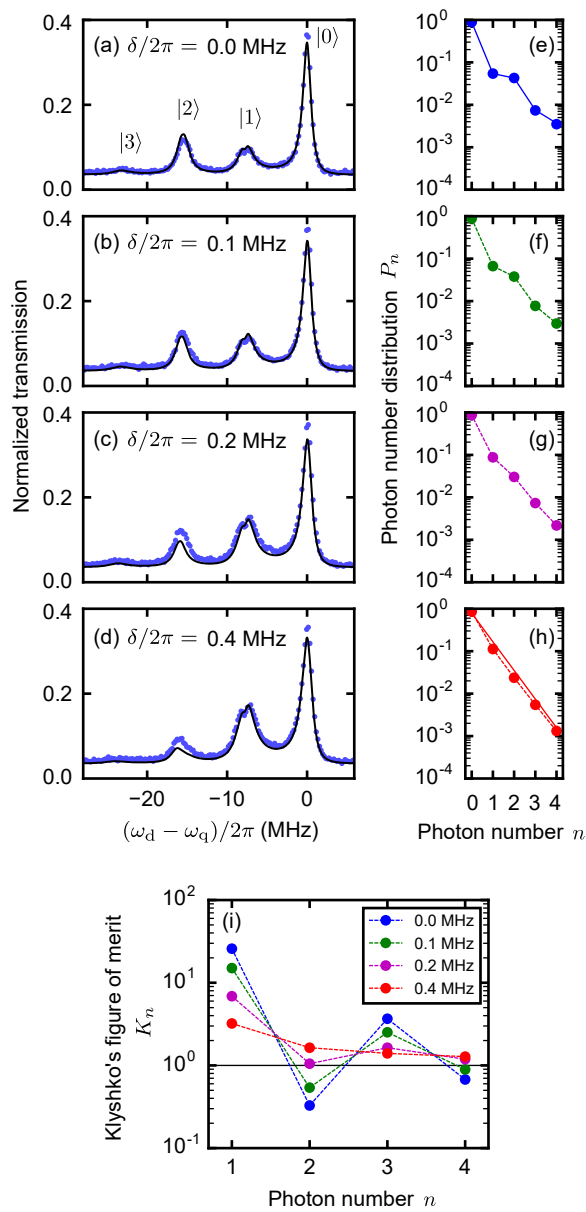


FIG. 4. (a)-(d) Squeezed-drive-frequency dependence of the qubit spectrum. $\delta = \omega_s - (\omega_c + \chi)$ is the detuning between the center frequency ω_s of the squeezed vacuum field and the cavity resonant frequency $\omega_c + \chi$. Blue dots are the experimental results, and black solid lines are the numerical calculations. (e)-(h) Photon number distributions determined from the fittings (dots and dashed lines). Solid lines in (e) and (h) are the photon number distributions calculated from the corresponding models. (i) Klyshko's figures of merit K_n evaluated for each detuning δ .

$n = 2$ and 4. Thus, the photon number distribution fulfills Klyshko's criterion for nonclassicality. In contrast, K_n 's for coherent states are all expected to be one. For the case with a coherent drive, the values are indeed close to one with a small excess due to the thermal background.

Finally, we study the squeezed-drive-frequency dependence of the qubit spectrum as shown in Figs. 4(a)-(d). When the detuning δ between the center frequency ω_s of the generated broadband squeezed vacuum field and the cavity resonant frequency $\omega_c + \chi$ is zero, both photons in a pair are injected into the cavity with an identical probability, so that the even-odd photon number oscillation is preserved. When the detuning is increased, however, the injection probabilities of the photon pairs are asymmetrically biased, and the photon number oscillation is weakened. In the large detuning limit, the cavity state becomes a thermal state. This can be understood from the fact that a two-mode squeezed vacuum state is reduced to a thermal state after tracing out one of the modes. In Fig. 4, we observe that the photon number oscillation is diminished as the detuning is increased. Eventually, the photon number distribution approaches the Boltzmann distribution of a thermal state with the average photon number $n_{\text{th}} = 0.27$ [red solid line in Fig. 4(h)]. These observations indicate that a broadband squeezed vacuum field has correlated photon pairs in frequency space. Klyshko's figures of merit plotted in Fig. 4(i) shows that the nonclassicality is reduced as the detuning is increased and that the cavity state becomes a classical state, i.e., $K_n > 1$ for any photon number n .

In conclusion, we developed a circuit-QED scheme to determine the photon number distribution in a cavity driven continuously. By analyzing the Stark-shifted qubit spectra, the photon number distributions are determined for the drive fields such as thermal, coherent, and squeezed vacuum states. Most importantly, the distribution under the squeezed vacuum drive is shown to fulfill Klyshko's criterion for nonclassicality. According to the input-output relation, the measurement scheme allows us to analyze the photon number distribution and the nonclassicality in the propagating microwave field.

We acknowledge the fruitful discussion with K. Wakui. This work was supported in part by the Project for Developing Innovation System of MEXT, ALPS, JSPS KAKENHI (No. 16K05497 and 26220601), and ERATO, JST.

SUPPLEMENTARY MATERIALS

S1. EXPERIMENTAL SETUP

The experimental setup is shown in Fig. S1. We use a circuit-QED architecture, where a transmon qubit is mounted at the center of a three-dimensional superconducting cavity. The three-dimensional superconducting cavity is made of aluminum (A1050). The transmon qubit with an Al/AIO_x/Al Josephson junction is fabricated on a silicon substrate. From the frequency-domain measurements (see Sec. S4 below), we determine the dressed cavity resonant frequency $\omega_c/2\pi = 10.4005$ GHz, the total cavity decay rate $\kappa/2\pi = 0.494$ MHz, and the effective dispersive shift $\chi/2\pi = 3.9$ MHz. The dressed qubit resonant frequency is $\omega_q/2\pi = 8.7941$ GHz, and the dressed anharmonicity is -136 MHz. By using the dressed frequencies, we find the bare cavity resonant frequency, 10.3660 GHz, and the coupling strength between the qubit and the cavity, 240 MHz. The bare qubit resonant frequency is 8.8320 GHz, and its anharmonicity is -140 MHz, corresponding to $E_J/E_C \approx 500$.

To determine the photon number distribution in the cavity that is driven continuously by various types of microwave fields, we observe the qubit spectra, which reflect the photon number distribution. The transmission of the cavity probe field ω_p is measured by using a vector network analyzer (VNA), while sweeping the qubit drive frequency ω_d . The qubit drive field ω_d is added to the input line at the directional coupler at room temperature. As the cavity drive field ω_s to generate the steady-state photon number distribution in the cavity, we use thermal states, coherent states, and squeezed vacuum states. A switch connects each source to the cavity, as shown in Fig. S1. Thermal states are generated by amplifying and filtering the thermal noise at room temperature and led to the cavity through attenuators. Coherent states are generated by a microwave source at room temperature and led to the cavity through attenuators to suppress the thermal background. Squeezed vacuum states are generated by pumping a flux-driven Josephson parametric amplifier (JPA) at twice the JPA resonant frequency [8, 31]. The JPA resonant frequency is tuned to the cavity resonant frequency with the qubit in the ground state by applying the DC magnetic field.

S2. THEORETICAL DESCRIPTION

In this section, we present the formula used in the numerical calculations. In the setup considered (Fig. S2), a qubit-cavity system (System A) is subject to a continuous squeezed vacuum field generated by a JPA (System B). Setting $\hbar = 1$, The Hamiltonian of System A with the

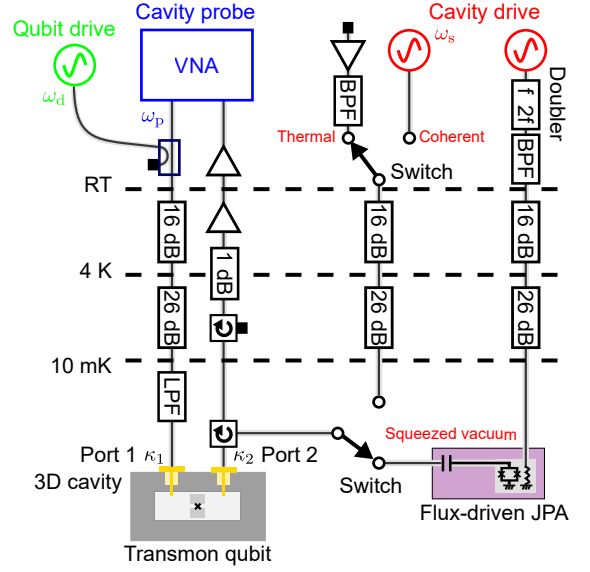


FIG. S1. Schematic of the experimental setup. $\omega_p = \omega_c - \chi$ is the cavity probe frequency, ω_d is the qubit drive frequency, and $\omega_s = \omega_c + \chi$ is the cavity drive frequency.

qubit drive and the cavity probe fields is described by

$$\begin{aligned} \mathcal{H} = & \omega_c a^\dagger a + \frac{\omega_q}{2} \sigma_z - \chi a^\dagger a \sigma_z + \frac{\Omega_d}{2} (e^{-i\omega_d t} \sigma^\dagger + e^{i\omega_d t} \sigma) \\ & + \frac{\Omega_p}{2} (e^{-i\omega_p t} a^\dagger + e^{i\omega_p t} a), \end{aligned} \quad (\text{S1})$$

where a and σ respectively denote the annihilation operators of the cavity mode and the qubit, $\sigma_z = \sigma^\dagger \sigma - \sigma \sigma^\dagger$, and Ω_d and Ω_p are the amplitudes of the qubit drive and the cavity probe, respectively. The Hamiltonian of System B is given by

$$\mathcal{H}' = \omega_s b^\dagger b + \frac{\Omega_s}{2} (e^{-2i\omega_s t} b^{\dagger 2} + e^{2i\omega_s t} b^2), \quad (\text{S2})$$

where b is the annihilation operator of the JPA mode, and ω_s is its frequency. We apply a pump field with frequency $2\omega_s$ and amplitude Ω_s to the JPA to generate a squeezed vacuum.

By taking the free Hamiltonian $\mathcal{H}_0 = \omega_s (a^\dagger a + b^\dagger b) + \frac{\omega_d}{2} \sigma_z$, we switch to the rotating frame. In this frame, \mathcal{H} and \mathcal{H}' are rewritten as

$$\begin{aligned} \mathcal{H} = & (\omega_c - \omega_s) a^\dagger a + \frac{(\omega_q - \omega_d)}{2} \sigma_z - \chi a^\dagger a \sigma_z \\ & + \frac{\Omega_d}{2} (\sigma^\dagger + \sigma) + \frac{\Omega_p}{2} (e^{-i(\omega_p - \omega_s)t} a^\dagger + e^{i(\omega_p - \omega_s)t} a), \end{aligned} \quad (\text{S3})$$

$$\mathcal{H}' = \frac{\Omega_s}{2} (b^{\dagger 2} + b^2). \quad (\text{S4})$$

The squeezed vacuum field generated by System B is guided to System A through a waveguide. We define a

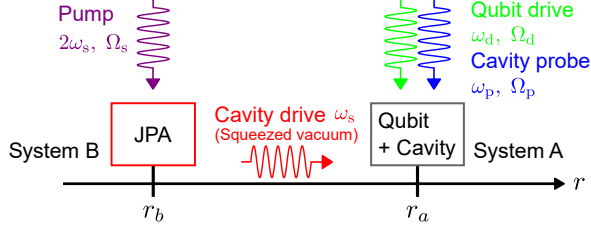


FIG. S2. Schematic of the model. The output field from System B (JPA) is used as the input for System A (qubit and cavity). The coordinate r is defined along the propagation direction of the waveguide field. A circulator placed between Systems A and B in the experiment (see Fig. S1) allows us to treat only the right-going mode in the calculation.

spatial coordinate r along with the propagating direction of the waveguide field (see Fig. S2). The waveguide field interacts with System A at r_a and System B at r_b . Setting the microwave velocity in the waveguide to unity, the overall Hamiltonian is written as

$$\begin{aligned} \mathcal{H}_{\text{total}} = & \mathcal{H} + \mathcal{H}' + \int dk kc_k^\dagger c_k \\ & + \sqrt{\kappa_e'} (b^\dagger \tilde{c}_{r_b} + \tilde{c}_{r_b}^\dagger b) + \sqrt{\kappa_e} (a^\dagger \tilde{c}_{r_a} + \tilde{c}_{r_a}^\dagger a), \end{aligned} \quad (\text{S5})$$

where c_k is the waveguide-field operator with wave number k , and κ_e (κ_e') represents the external coupling of System A (B) to the waveguide field. \tilde{c}_r is the spatial representation of the waveguide-field operator, as given by $\tilde{c}_r = (2\pi)^{-1/2} \int dk e^{ikr} c_k$. Note that the photon frequency should be measured relative to ω_s , since we are in the rotating frame.

We denote an arbitrary operator belonging to System A (B) by S_A (S_B) and investigate its time evolution at t ($t-l$), where $l = r_a - r_b (> 0)$ is the distance between the two systems. This is because $S_A(t)$ and $S_B(t-l)$ are on the same light cone and are therefore relativistically simultaneous. From Eq. (S5), we can derive the following Heisenberg equations,

$$\begin{aligned} \frac{d}{dt} S_A = & i[\mathcal{H}, S_A] + i\sqrt{\kappa_e} [a^\dagger, S_A] \tilde{c}_{r_a}(t) \\ & + i\sqrt{\kappa_e} \tilde{c}_{r_a}^\dagger(t) [a, S_A], \end{aligned} \quad (\text{S6})$$

$$\begin{aligned} \frac{d}{dt} S_B = & i[\mathcal{H}', S_B] + i\sqrt{\kappa_e'} [b^\dagger, S_B] \tilde{c}_{r_b}(t-l) \\ & + i\sqrt{\kappa_e'} \tilde{c}_{r_b}^\dagger(t-l) [b, S_B], \end{aligned} \quad (\text{S7})$$

and the input-output relation,

$$\begin{aligned} \tilde{c}_r(t) = & \tilde{c}_{r-t}(0) \\ & - i\sqrt{\kappa_e'} \theta(r-r_b) \theta(t-r+r_b) b(t-r+r_b) \\ & - i\sqrt{\kappa_e} \theta(r-r_a) \theta(t-r+r_a) a(t-r+r_a), \end{aligned} \quad (\text{S8})$$

where $\theta(t)$ is the step function. Since we analyze the stationary response, we assume that t is sufficiently large. Therefore, $\tilde{c}_{r_b}(t-l) = \tilde{c}_{r_a-t}(0) - i\sqrt{\kappa_e'} b(t-l)/2$ and $\tilde{c}_{r_a}(t) = \tilde{c}_{r_a-t}(0) - i\sqrt{\kappa_e} a(t)/2 - i\sqrt{\kappa_e'} b(t-l)$. From these equations, Eqs. (S6) and (S7) are rewritten as

$$\begin{aligned} \frac{d}{dt} S_A = & i[\mathcal{H}, S_A] + \frac{\kappa_e}{2} \mathcal{L}_a[S_A] \\ & + \sqrt{\kappa_e \kappa_e'} [a^\dagger, S_A] b + \sqrt{\kappa_e \kappa_e'} b^\dagger [S_A, a] \\ & + i\sqrt{\kappa_e} [a^\dagger, S_A] \tilde{c}_{r_a-t}(0) + i\sqrt{\kappa_e} \tilde{c}_{r_a-t}^\dagger(0) [a, S_A], \end{aligned} \quad (\text{S9})$$

$$\begin{aligned} \frac{d}{dt} S_B = & i[\mathcal{H}', S_B] + \frac{\kappa_e'}{2} \mathcal{L}_b[S_B] \\ & + i\sqrt{\kappa_e'} [b^\dagger, S_B] \tilde{c}_{r_a-t}(0) + i\sqrt{\kappa_e'} \tilde{c}_{r_a-t}^\dagger(0) [b, S_B], \end{aligned} \quad (\text{S10})$$

where $\mathcal{L}_a[S_A] = [a^\dagger, S_A]a + a^\dagger[S_A, a]$. The Heisenberg equation for the product operator $S_B S_A$ can be derived from Eqs. (S9) and (S10). Care should be taken that $[\tilde{c}_{r_a-t}(0), S_B(t-l)] = i\sqrt{\kappa_e'} [b(t-l), S_B(t-l)]/2$ and $[\tilde{c}_{r_a-t}(0), S_A(t)] = i\sqrt{\kappa_e} [a(t), S_A(t)]/2$, both of which result from Eq. (S8). In the considered setup, we do not apply an input field to System A through the waveguide. Therefore, denoting the initial state vector of the overall system by $|\psi_i\rangle$, we can rigorously take $\tilde{c}_r(0)|\psi_i\rangle = 0$. Then, the equation of motion for $\langle S_A S_B \rangle = \langle \psi_i | S_A S_B | \psi_i \rangle$ is written as

$$\begin{aligned} \frac{d}{dt} \langle S_A S_B \rangle = & i\langle [\mathcal{H}, S_A] S_B \rangle + i\langle S_A [\mathcal{H}', S_B] \rangle \\ & + \sqrt{\kappa_e \kappa_e'} \langle [S_A, a] b^\dagger S_B \rangle + \sqrt{\kappa_e \kappa_e'} \langle [a^\dagger, S_A] S_B b \rangle \\ & + \frac{\kappa_e}{2} \langle \mathcal{L}_a[S_A] S_B \rangle + \frac{\kappa_e'}{2} \langle S_A \mathcal{L}_b[S_B] \rangle. \end{aligned} \quad (\text{S11})$$

Up to here, we assumed for simplicity that Systems A and B damp only through the radiative coupling to the waveguide field. Here, we include other dissipation channels, such as the decay of cavities A and B into other environments, and the decay and pure dephasing of the qubit in System A. Furthermore, we take account of the thermal excitation of the systems through the environment. Then, Eq. (S11) should be replaced with the following one,

$$\begin{aligned} \frac{d}{dt} \langle S_A S_B \rangle = & i\langle [\mathcal{H}, S_A] S_B \rangle + i\langle S_A [\mathcal{H}', S_B] \rangle \\ & + \sqrt{\kappa_e \kappa_e'} \langle [S_A, a] b^\dagger S_B \rangle + \sqrt{\kappa_e \kappa_e'} \langle [a^\dagger, S_A] S_B b \rangle \\ & + \frac{\kappa_e'}{2} \langle S_A \mathcal{L}_b[S_B] \rangle + \frac{\kappa(1+n_{\text{th}})}{2} \langle \mathcal{L}_a[S_A] S_B \rangle \\ & + \frac{\kappa n_{\text{th}}}{2} \langle \mathcal{L}_{a^\dagger}[S_A] S_B \rangle + \frac{\gamma(1+p_{\text{th}})}{2} \langle \mathcal{L}_\sigma[S_A] S_B \rangle \\ & + \frac{\gamma p_{\text{th}}}{2} \langle \mathcal{L}_{\sigma^\dagger}[S_A] S_B \rangle + \frac{\gamma}{2} \langle \mathcal{L}_{\sigma^\dagger \sigma}[S_A] S_B \rangle. \end{aligned} \quad (\text{S12})$$

where κ is the total cavity decay, n_{th} is the average thermal photon number in the cavity, $\gamma = 1/T_1$ is the qubit

decay rate, p_{th} is the thermal excitation probability of the qubit, and γ_ϕ is the qubit pure dephasing rate. Note that the internal loss and the thermal photon excitation of the JPA mode are neglected in Eq. (S12).

In the Fock-state basis, the state vector of the composite system is written as $|q, n, m\rangle$, where $q(=g, e)$ denotes the qubit state in System A, and n and $m(=0, 1, \dots)$ denotes the cavity photon numbers in Systems A and B, respectively. The density matrix of the composite system is obtained by setting $S_A S_B = S_{qnm, q'n'm'} = |q, n, m\rangle\langle q', n', m'|$ in Eq. (S12). Since the probe field is weak, we solve this equation perturbatively in Ω_p . For this purpose, we first determine the steady-state solution $\langle S_{qnm, q'n'm'} \rangle^{(0)}$ by setting $\Omega_p = 0$ in Eq. (S12). Then, we determine the linear response $\langle S_{qnm, q'n'm'} \rangle^{(1)}$, which is proportional to $\Omega_p e^{-i(\omega_p - \omega_d)t}$. Since the output probe field is measured at a different port (Port 2 in Fig. S1) from the input one (Port 1 in Fig. S1), the probe transmission coefficient is proportional to the cavity amplitude of System A, $\langle a \rangle^{(1)} = \sum_{q, n, m} \sqrt{n+1} \langle S_{qnm, q(n+1)m} \rangle^{(1)}$. The parameters used in the numerical calculations are shown in Table S1.

The parameters characterizing the cavity drive fields (thermal, coherent, and squeezed vacuum states) are determined by fitting the qubit spectrum with numerical results from Eq. (S12). Then, the photon number distribution is determined from Eq. (S12) in absence of the qubit drive and cavity probe fields ($\Omega_d = \Omega_p = 0$). When a thermal state is applied as the cavity drive field, the average thermal photon number n_{th} is used as the fitting parameter. When a coherent state is used as the cavity drive, the Hamiltonian of System B is replaced with

$$\mathcal{H}' = \frac{\Omega_s}{2} (b^\dagger + b). \quad (\text{S13})$$

Then, the output field from System B becomes a coherent state. The amplitude Ω_s , corresponding to the strength of the coherent drive to the cavity, is used as an addi-

TABLE S1. System parameters.

Dressed cavity transition frequency	$\omega_c/2\pi$	10.4005 GHz
Cavity external coupling rate	$\kappa_e/2\pi$	0.490 MHz
Cavity total decay rate	$\kappa/2\pi$	0.494 MHz
Thermal average photon number	n_{th}	0.04
Cavity probe amplitude	$\Omega_p/2\pi$	0.16 MHz
Dressed qubit transition frequency	$\omega_q/2\pi$	8.7941 GHz
Qubit decay rate	$\gamma = 1/T_1$	$1/5.5 \mu\text{s}^{-1}$
Qubit dephasing rate	γ_ϕ	0
Thermal excitation probability	p_{th}	0.01
Qubit drive amplitude	$\Omega_d/2\pi$	0.46 MHz
Effective dispersive shift	$\chi/2\pi$	3.9 MHz
JPA external (total) coupling rate	$\kappa'_e/2\pi$	40 MHz

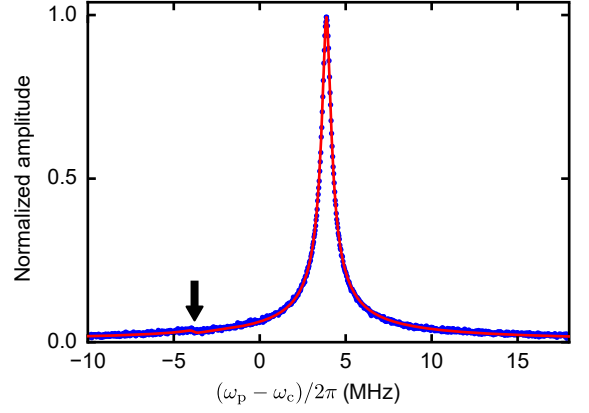


FIG. S3. Cavity transmission as a function of the cavity probe frequency ω_p . The amplitude is normalized by the maximum peak value. This normalization factor is used commonly all through the paper. The main peak at $\omega_p = \omega_c + \chi$ corresponds to the cavity resonance with the qubit in the ground state. The small cavity peak at $\omega_p = \omega_c - \chi$ (arrow), corresponding to the qubit excited state, is also observed due to the thermal excitation of the qubit. Red solid line represents the numerical result.

tional fitting parameter. For the case with a squeezed vacuum drive, we need to incorporate the loss of waveguide between the JPA and the cavity, since the squeezed vacuum state is degraded considerably by the loss of the waveguide. Theoretically, such waveguide loss is taken into account by decreasing the coupling κ_e between the waveguide and the cavity of System A while keeping its total decay rate κ . Accordingly, the pump amplitude for the JPA, Ω_s , and the external coupling rate of the cavity, κ_e , are used as the fitting parameters. In the numerical simulations in Fig. 3 of the main text, we employed the following parameters: $n_{\text{th}} = 0.22$ in Fig. 3(a), $\Omega_s/2\pi = 1.3$ MHz in Fig. 3(b), and $\Omega_s/2\pi = 4.0$ MHz and $\kappa_e/2\pi = 0.42$ MHz in Fig. 3(c).

S3. PHOTON NUMBER DISTRIBUTION

Throughout this work, we determine the cavity photon number distribution numerically, based on the framework described in Sec. 2. In order to characterize these quantum states more intuitively, we here employ the single-mode density matrices and evaluate their photon number distributions. When the classical fields, such as thermal and coherent states, are applied to the cavity, the cavity state is described by a thermal coherent state, whose density matrix ρ_{tc} is given by

$$\rho_{\text{tc}} = \mathcal{D}(\alpha) \rho(n_{\text{th}}) \mathcal{D}^\dagger(\alpha), \quad (\text{S14})$$

where $\mathcal{D}(\alpha) = \exp(\alpha a^\dagger - \alpha^* a)$ is the displacement operator with a parameter α , and $\rho(n_{\text{th}}) \propto \left(\frac{n_{\text{th}}}{1+n_{\text{th}}}\right)^{a^\dagger a}$ is

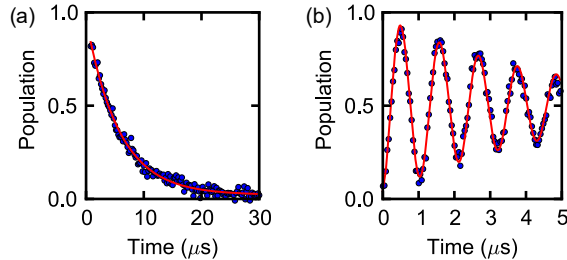


FIG. S4. Time-domain measurements of the qubit coherence. (a) Relaxation of the qubit. Red solid line is a fit to an exponential curve with $T_1 = 5.5 \mu\text{s}$. (b) Dephasing of the qubit. T_2^* is $4.5 \mu\text{s}$. Red solid line is the numerical result with $n_{\text{th}} = 0.04$.

the thermal-state density matrix with the average photon number n_{th} . In Figs. 3(a) and (b) of the main text, we plot the photon number distribution calculated from Eq. (S14) by solid lines. We find the cavity state for the thermal drive corresponds to a thermal coherent state with $|\alpha| = 0.0$ and $n_{\text{th}} = 0.22$, which is an exact thermal state. In the same way, the cavity state for the coherent cavity drive is fitted by a thermal coherent state with $|\alpha| = 0.49$ and $n_{\text{th}} = 0.04$. The finite thermal photon population is due to the background noise from room temperature. For the squeezed cavity drive, we assume the following density matrix,

$$\rho_{\text{sq}} = \text{Tr}_{a'} \left[\mathcal{U}_{\text{BS}}(\theta) \rho(r) \otimes \rho'_0 \mathcal{U}_{\text{BS}}^\dagger(\theta) \right], \quad (\text{S15})$$

where $\rho(r) = \mathcal{S}(r)|0\rangle\langle 0|\mathcal{S}^\dagger(r)$ [$\mathcal{S}(r) = \exp\left(\frac{r}{2}(a^2 - a'^{\dagger 2})\right)$] is a squeezed vacuum state of the cavity mode a with a squeezing parameter r , ρ'_0 is a vacuum state of an ancilla mode a' , $\mathcal{U}_{\text{BS}}(\theta) = \exp\left(-\frac{\theta}{2}(aa'^{\dagger} + a'^{\dagger}a)\right)$ is a unitary operator describing a beam splitter with a loss rate of $l = \sin\theta$, and $\text{Tr}_{a'}$ is a partial trace for the ancilla mode a' . By fitting the photon number distribution with this theoretical model, we find the cavity quantum state with the squeezed drive corresponds to a squeezed vacuum state ($r = 0.54$) with a loss ($l = 0.42$).

S4. SYSTEM PARAMETERS

In this section, we explain how we determined the parameters used in the previous sections. Since the cavity drive field ω_s is absent here, we take a rotating frame determined by $\mathcal{H}_0 = \omega_p a^\dagger a + \frac{\omega_d}{2} \sigma_z$. Then, the Hamiltonian Eq. (S1) is rewritten as

$$\mathcal{H} = (\omega_c - \omega_p) a^\dagger a + \frac{(\omega_q - \omega_d)}{2} \sigma_z - \chi a^\dagger a \sigma_z + \frac{\Omega_d}{2} (\sigma^\dagger + \sigma) + \frac{\Omega_p}{2} (a^\dagger + a). \quad (\text{S16})$$

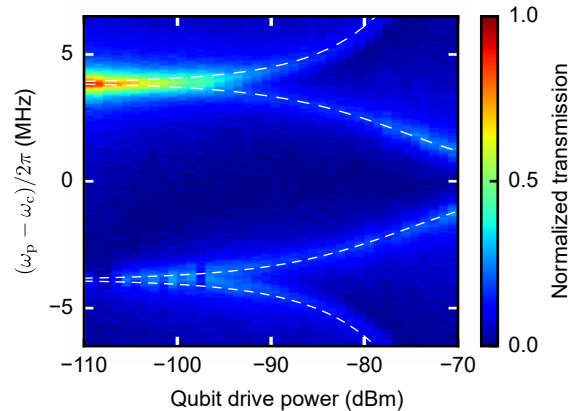


FIG. S5. Cavity transmission as a function of the cavity probe frequency ω_p and the qubit drive power Ω_d . White dashed lines depict the observed cavity resonances.

By using Eq. (S12) with $S_B = \hat{1}$ and $\kappa'_e = 0$, we calculate the time-evolution and the steady-state solutions of System A. They correspond to the solution of the conventional system-bath master equation of System A.

First, the cavity transmission amplitude, measured as a function of the cavity probe frequency ω_p in the absence of any drive field, is shown in Fig. S3. The cavity resonance is observed at the probe power corresponding to the single photon level. The main peak at $\omega_p = \omega_c + \chi$ is the cavity resonance with the qubit in the ground state. In addition, the small peak corresponding to the cavity with the qubit excited state is also observed at $\omega_p = \omega_c - \chi$ due to the finite thermal excitation probability of the qubit, p_{th} . Red solid line is calculated from the steady-state solution of Eq. (S12), by setting $S_A = a$. From this, we find $p_{\text{th}} = 0.01$.

Next, time-domain measurements are conducted to evaluate the coherence of the qubit. A DAC-ADC system, instead of the VNA in Fig. S1, is used for the measurement. The results of the qubit relaxation and Ramsey decay measurements are shown in Figs. S4(a) and (b). We obtain $T_1 = 5.5 \mu\text{s}$, $T_2^* = 4.5 \mu\text{s}$ by fitting the data. The total dephasing rate of the qubit $1/T_2^*$ is described with $\gamma/2 + \gamma_\phi + \gamma_{\text{th}}$, where $\gamma_{\text{th}} = \frac{4\kappa\chi^2}{\kappa^2 + \chi^2} n_{\text{th}}$ is the dephasing rate due to the thermal photon fluctuation in the cavity [32]. Assuming $\gamma_\phi = 0$, the thermal average photon number n_{th} in the cavity is determined to be 0.04 by using the simple formula. Red solid line in Fig. S3(b) is the time-evolution solution of Eq. (S12), by setting $S_A = (\sigma_z + 1)/2$, where $(\omega_q - \omega_d)/2\pi = 0.9 \text{ MHz}$, $\Omega_d = \Omega_p = 0$, and $n_{\text{th}} = 0.04$ are used. The calculation reproduces well the experimental result.

In order to calibrate the qubit drive power, the cavity transmission, measured as a function of the cavity probe frequency ω_p and the qubit drive power Ω_d , is shown in Fig. S5. The qubit drive frequency ω_d is in resonance

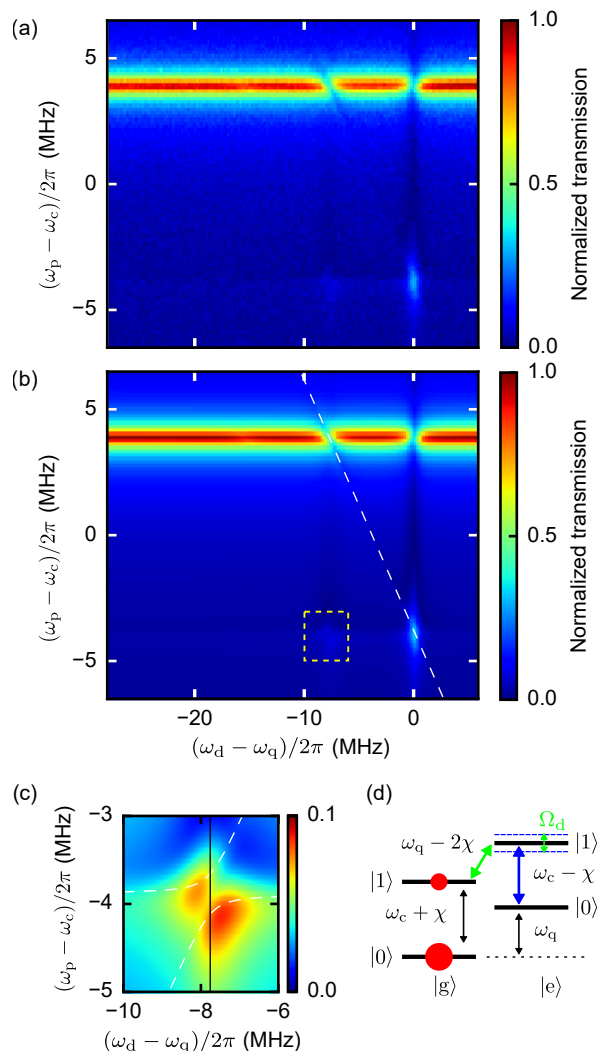


FIG. S6. Cavity transmission as a function of the qubit drive frequency ω_d and the cavity probe frequency ω_p . (a) Experimental data. (b) Steady-state solutions of Eq. (S12). Diagonal dashed line corresponds to the resonant condition for the two-photon transition, $\omega_p + \omega_d = \omega_c + \omega_q - \chi$. (c) Magnified plot of the region in yellow dashed rectangle in (b) at around $\omega_p = \omega_c - \chi$ and $\omega_d = \omega_q - 2\chi$. White dashed lines depict the calculated transition frequencies between $|e, 0\rangle$ and the hybridized states composed of $|e, 1\rangle$ and $|g, 1\rangle$. Black solid line indicates $\omega_d = \omega_q - 2\chi$, corresponding to the qubit transition frequency with the single photon state in the cavity. (d) Energy levels of the dispersively coupled qubit-cavity system with the qubit drive field. $|e, 1\rangle$ and $|g, 1\rangle$ are hybridized by the qubit drive.

with the qubit resonant frequency ω_q . As the qubit drive power increases, the cavity peak corresponding to the qubit in the excited state appears, and each peak splits into two peaks due to Rabi splitting of the qubit. In this experiment, the cavity probe power is weak enough to excite at most the single photon state in the cavity. Therefore, the four resonances in Fig S5 correspond

to the transitions between the lowest eigen frequencies: $\omega_{0\pm} = \pm \frac{\Omega_d}{2}$ and $\omega_{1\pm} = \omega_c \pm \sqrt{\chi^2 + (\frac{\Omega_d}{2})^2}$, which are calculated from the Hamiltonian Eq. (S16) with $\omega_d = \omega_q$ and $\omega_p = \Omega_p = 0$. White dashed lines in Fig. S5 depict these transition frequencies and agree with the observed resonance peaks. With this plot, we performed the calibration between the actual qubit drive power and Ω_d . The qubit drive power -97 dBm at sample, that we use for the measurement of the qubit spectroscopy, corresponds to $\Omega_d/2\pi = 0.46$ MHz.

In order to calibrate the cavity probe power, we use the qubit spectra at $\omega_p = \omega_c \pm \chi$, as shown in Fig. 2(b) of the main text. Red (blue) dots plot the cavity transmission as a function of the qubit drive frequency ω_d , fixing the cavity probe frequency $\omega_p = \omega_c + \chi$ ($\omega_p = \omega_c - \chi$). The qubit spectra strongly reflect the cavity probe power Ω_p and the average thermal photon number n_{th} in the cavity. Green solid lines are the steady-state solution of Eq. (S12), by setting $S_A = a$. From the simulations, we find the cavity probe power -125 dBm at sample, that we use for the qubit spectroscopy, corresponds to $\Omega_p/2\pi = 0.16$ MHz. The average thermal photon number n_{th} , which is determined from T_2^* measurement, agrees well with the qubit spectra.

Using these parameters, listed in Table S1, the cavity transmission as a function of the qubit drive frequency ω_d the cavity probe frequency ω_p are numerically calculated from the steady-state solution of Eq. (S12), by setting $S_A = a$, as shown in Fig. S6. The calculation results agree well with the experimental results, which assures the accuracy in the determination of the parameters.

In the qubit spectrum for $\omega_p = \omega_c - \chi$ [Fig. 2(a)], we find a splitting in the peak corresponding to the single photon occupancy. The splitting is understood as the Autler-Townes effect involving the three states: $|e, 0\rangle$, $|e, 1\rangle$ and $|g, 1\rangle$ [33]. In the cavity probe frequency ω_p dependence of the qubit spectra, an anti-crossing like splitting is observed at around $\omega_p = \omega_c - \chi$ and $\omega_d = \omega_q - 2\chi$, as shown in the yellow rectangle in Fig. S6(b) and in Fig. S6(c). Due to the thermal photon excitation in the cavity, the population of $|g, 1\rangle$ is finite. In the steady-state, the qubit drive field at $\omega_d = \omega_q - 2\chi$ transfers the population of $|g, 1\rangle$ to $|e, 0\rangle$, because the cavity decay rate κ is larger than the qubit Rabi frequency Ω_d and the qubit decay rate γ . Therefore, the cavity probe field around $\omega_p = \omega_c - \chi$ can excite the photons in the cavity from $|e, 0\rangle$. The qubit drive field couples $|e, 1\rangle$ to $|g, 1\rangle$ and splits the spectrum into the two peaks with the separation of Ω_d [see fig. S6(d)]. White dashed lines in Fig. S6(c) depict the transition frequencies from $|e, 0\rangle$ to the hybridized states composed of $|g, 1\rangle$ and $|e, 1\rangle$, which is calculated from the Hamiltonian Eq. (S16) with $\omega_p = \Omega_p = 0$.

-
- [1] M. H. Devoret and R. J. Schoelkopf, *Science* **339**, 1169 (2013).
- [2] A. Blais, R.-S. Huang, A. Wallraff, S. M. Girvin, and R. J. Schoelkopf, *Phys. Rev. A* **69**, 062320 (2004).
- [3] P. D. Drummond and Z. Ficek, *Quantum Squeezing*, Vol. 27 (Springer Science & Business Media, 2013).
- [4] R. Movshovich, B. Yurke, P. G. Kaminsky, A. D. Smith, A. H. Silver, R. W. Simon, and M. V. Schneider, *Phys. Rev. Lett.* **65**, 1419 (1990).
- [5] M. Castellanos-Beltran, K. Irwin, G. Hilton, L. Vale, and K. Lehnert, *Nature Phys.* **4**, 929 (2008).
- [6] F. Mallet, M. A. Castellanos-Beltran, H. S. Ku, S. Glancy, E. Knill, K. D. Irwin, G. C. Hilton, L. R. Vale, and K. W. Lehnert, *Phys. Rev. Lett.* **106**, 220502 (2011).
- [7] E. P. Menzel, R. Di Candia, F. Deppe, P. Eder, L. Zhong, M. Ihmig, M. Haerberlein, A. Baust, E. Hoffmann, D. Ballester, K. Inomata, T. Yamamoto, Y. Nakamura, E. Solano, A. Marx, and R. Gross, *Phys. Rev. Lett.* **109**, 250502 (2012).
- [8] L. Zhong, E. P. Menzel, R. Di Candia, P. Eder, M. Ihmig, A. Baust, M. Haerberlein, E. Hoffmann, K. Inomata, T. Yamamoto, Y. Nakamura, E. Solano, F. Deppe, A. Marx, and R. Gross, *New J. Phys.* **15**, 125013 (2013).
- [9] C. M. Wilson, G. Johansson, A. Pourkabirian, M. Simoen, J. R. Johansson, T. Duty, F. Nori, and P. Delsing, *Nature* **479**, 376 (2011).
- [10] C. Eichler, D. Bozyigit, C. Lang, M. Baur, L. Steffen, J. M. Fink, S. Filipp, and A. Wallraff, *Phys. Rev. Lett.* **107**, 113601 (2011).
- [11] N. Bergeal, F. Schackert, L. Frunzio, and M. H. Devoret, *Phys. Rev. Lett.* **108**, 123902 (2012).
- [12] E. Flurin, N. Roch, F. Mallet, M. H. Devoret, and B. Huard, *Phys. Rev. Lett.* **109**, 183901 (2012).
- [13] C. Macklin, K. O'Brien, D. Hover, M. E. Schwartz, V. Bolkhovskiy, X. Zhang, W. D. Oliver, and I. Siddiqi, *Science* **350**, 307 (2015).
- [14] K. W. Murch, S. J. Weber, K. M. Beck, E. Ginossar, and I. Siddiqi, *Nature* **499**, 62 (2013).
- [15] D. M. Toyli, A. W. Eddins, S. Boutin, S. Puri, D. Hover, V. Bolkhovskiy, W. D. Oliver, A. Blais, and I. Siddiqi, *Phys. Rev. X* **6**, 031004 (2016).
- [16] A. Bienfait, P. Campagne-Ibarcq, A. Holm-Kiilerich, X. Zhou, S. Probst, J. J. Pla, T. Schenkel, D. Vion, D. Esteve, J. J. L. Morton, K. Moelmer, and P. Bertet, arXiv:1610.03329 (2016).
- [17] W. Schleich and J. Wheeler, *Nature* **326**, 574 (1987).
- [18] E. Waks, B. C. Sanders, E. Diamanti, and Y. Yamamoto, *Phys. Rev. A* **73**, 033814 (2006).
- [19] K. Wakui, Y. Eto, H. Benichi, S. Izumi, T. Yanagida, K. Ema, T. Numata, D. Fukuda, M. Takeoka, and M. Sasaki, *Sci. Rep.* **4**, 4535 (2014).
- [20] Y.-F. Chen, D. Hover, S. Sendelbach, L. Maurer, S. T. Merkel, E. J. Pritchett, F. K. Wilhelm, and R. McDermott, *Phys. Rev. Lett* **107**, 217401 (2011).
- [21] K. Inomata, Z. Lin, K. Koshino, W. D. Oliver, J. S. Tsai, T. Yamamoto, and Y. Nakamura, *Nature Commun.* **7**, 12303 (2016).
- [22] A. Narla, S. Shankar, M. Hatridge, Z. Leghtas, K. M. Sliwa, E. Zalys-Geller, S. O. Mundhada, W. Pfaff, L. Frunzio, R. J. Schoelkopf, and M. H. Devoret, *Phys. Rev. X* **6**, 031036 (2016).
- [23] D. I. Schuster, A. A. Houck, J. A. Schreier, A. Wallraff, J. M. Gambetta, A. Blais, L. Frunzio, J. Majer, B. Johnson, M. H. Devoret, S. H. Girvin, and R. J. Schoelkopf, *Nature* **445**, 515 (2007).
- [24] B. Suri, Z. K. Keane, L. S. Bishop, S. Novikov, F. C. Wellstood, and B. S. Palmer, *Phys. Rev. A* **92**, 063801 (2015).
- [25] J. Gambetta, A. Blais, D. I. Schuster, A. Wallraff, L. Frunzio, J. Majer, M. H. Devoret, S. M. Girvin, and R. J. Schoelkopf, *Phys. Rev. A* **74**, 042318 (2006).
- [26] D. N. Klyshko, *Phys. Lett. A* **213**, 7 (1996).
- [27] A. A. Clerk, M. H. Devoret, S. M. Girvin, F. Marquardt, and R. J. Schoelkopf, *Rev. Mod. Phys.* **82**, 1155 (2010).
- [28] M. Hofheinz, H. Wang, M. Ansmann, R. C. Bialczak, E. Lucero, M. Neeley, A. D. O'Connell, D. Sank, J. Wenner, J. M. Martinis, and A. N. Cleland, *Nature* **459**, 546 (2009).
- [29] B. Vlastakis, G. Kirchmair, Z. Leghtas, S. E. Nigg, L. Frunzio, S. M. Girvin, M. Mirrahimi, M. H. Devoret, and R. J. Schoelkopf, *Science* **342**, 607 (2013).
- [30] See accompanying supplementary materials for details.
- [31] T. Yamamoto, K. Inomata, M. Watanabe, K. Matsuba, T. Miyazaki, W. Oliver, Y. Nakamura, and J. Tsai, *Appl. Phys. Lett.* **93**, 042510 (2008).
- [32] A. A. Clerk and D. W. Utami, *Phys. Rev. A* **75**, 042302 (2007).
- [33] B. Suri, Z. K. Keane, R. Ruskov, L. S. Bishop, C. Tahan, S. Novikov, J. E. Robinson, F. C. Wellstood, and B. S. Palmer, *New J. of Phys.* **15**, 125007 (2013).